

# UC San Diego

## UC San Diego Previously Published Works

### Title

Laser-driven acceleration of quasi-monoenergetic, near-collimated titanium ions via a transparency-enhanced acceleration scheme

### Permalink

<https://escholarship.org/uc/item/4j3581ff>

### Journal

New Journal of Physics, 21(10)

### ISSN

1367-2630

### Authors

Li, J  
Forestier-Colleoni, P  
Bailly-Grandvaux, M  
et al.

### Publication Date

2019-10-01

### DOI

10.1088/1367-2630/ab4454

Peer reviewed

PAPER • OPEN ACCESS

## Laser-driven acceleration of quasi-monoenergetic, near-collimated titanium ions via a transparency-enhanced acceleration scheme

To cite this article: J Li *et al* 2019 *New J. Phys.* **21** 103005

View the [article online](#) for updates and enhancements.



## PAPER






## Laser-driven acceleration of quasi-monoenergetic, near-collimated titanium ions via a transparency-enhanced acceleration scheme

## OPEN ACCESS

RECEIVED  
23 April 2019REVISED  
30 August 2019ACCEPTED FOR PUBLICATION  
13 September 2019PUBLISHED  
1 October 2019

Original content from this work may be used under the terms of the [Creative Commons Attribution 3.0 licence](#).

Any further distribution of this work must maintain attribution to the author(s) and the title of the work, journal citation and DOI.

J Li<sup>1</sup> , P Forestier-Colleoni<sup>1</sup>, M Bailly-Grandvaux<sup>1</sup> , C McGuffey<sup>1</sup>, A V Arefiev<sup>1</sup> , S S Bulanov<sup>2</sup>, J Peebles<sup>1</sup>, C Krauland<sup>1</sup>, A E Hussein<sup>3</sup> , T Batson<sup>3</sup>, J C Fernandez<sup>4</sup>, S Palaniyappan<sup>4</sup>, R P Johnson<sup>4</sup>, G M Petrov<sup>5</sup> and F N Beg<sup>1</sup> <sup>1</sup> Center for Energy Research, Univ. California San Diego, La Jolla, CA 92093-0417, United States of America<sup>2</sup> Lawrence Berkeley National Laboratory, Berkeley, CA 94720, United States of America<sup>3</sup> Center for Ultrafast Optical Science, Univ. of Michigan, Ann Arbor, MI 48109, United States of America<sup>4</sup> Los Alamos National Laboratory, Los Alamos, NM 87545, United States of America<sup>5</sup> Naval Research Laboratory, Plasma Physics Division, Washington, DC 20375, United States of AmericaE-mail: [fbeg@ucsd.edu](mailto:fbeg@ucsd.edu)**Keywords:** laser–plasma interactions, particle acceleration, ion beam generationSupplementary material for this article is available [online](#)**Abstract**

Laser-driven ion acceleration has been an active research area in the past two decades with the prospects of designing novel and compact ion accelerators. Many potential applications in science and industry require high-quality, energetic ion beams with low divergence and narrow energy spread. Intense laser ion acceleration research strives to meet these challenges and may provide high charge state beams, with some successes for carbon and lighter ions. Here we demonstrate the generation of well collimated, quasi-monoenergetic titanium ions with energies  $\sim 145$  and  $180$  MeV in experiments using the high-contrast ( $< 10^{-9}$ ) and high-intensity ( $6 \times 10^{20}$  W cm $^{-2}$ ) Trident laser and ultra-thin ( $\sim 100$  nm) titanium foil targets. Numerical simulations show that the foils become transparent to the laser pulses, undergoing relativistically induced transparency (RIT), resulting in a two-stage acceleration process which lasts until  $\sim 2$  ps after the onset of RIT. Such long acceleration time in the self-generated electric fields in the expanding plasma enables the formation of the quasi-monoenergetic peaks. This work contributes to the better understanding of the acceleration of heavier ions in the RIT regime, towards the development of next generation laser-based ion accelerators for various applications.

**1. Introduction**

Generation of high-intensity ion beams driven by short pulse lasers has emerged as an important area of laser–plasma research [1–3] due to the unique properties of intense short duration ion beams, which can be used for fast isochoric heating of dense matter [4–6]. For example, reaching the warm dense matter [7] conditions is relevant to laboratory astrophysics [8–10], geophysics [11, 12] and ion fast ignition of thermonuclear fuel targets [13–15]. Over the past 20 years, there was notably tremendous effort to understand the underlying physics of proton and light ion acceleration. However, there are limited efforts toward understanding laser acceleration of heavier ions [16–19], despite their potential for numerous applications in industry, medical and defense fields including generation of x-ray and gamma-ray radiation, nuclear reactions, and radiation effects in materials [20–23]. Still, the set of laser and target parameters most amenable to accelerate heavy ions is yet to be optimized, motivating the exploration of new acceleration mechanisms more suitable to produce monoenergetic/narrow-band and low-emittance heavy ion beams.

The most-studied acceleration mechanism, Target Normal Sheath Acceleration (TNSA) [24–26], is very robust and was shown to generate reproducible exponential energy spectrum of light-ions originating from the contaminants located at the target rear-side. Yet, this mechanism is inefficient in accelerating low-divergent and

narrow energy band ions, as well as ions heavier than carbon. With the recent development of high-power lasers, several new mechanisms have been identified. Two of the most promising advanced ion acceleration mechanisms are Radiation Pressure Acceleration (RPA) [27–31] and Relativistically Induced Transparency (RIT) [32–38]. RPA can potentially produce monoenergetic ion beams of higher energy than TNSA ( $E_{\max} \sim I^2$  for non-relativistic regime RPA compared to  $E_{\max} \sim I^{1/2}$  for TNSA [3], where  $E_{\max}$  is the maximum ion energy and  $I$  is the laser intensity) by driving forward a slab of plasma like a piston. Unfortunately, at the required ultrahigh intensities to trigger RPA as the main acceleration mechanism ( $I > 10^{22} \text{ W cm}^{-2}$ ), the ultra-thin target does not easily remain flat and opaque. First, the unwanted energy preceding the main pulse ionizes the target front surface, causing a plasma to expand into vacuum. Due to this expansion, the areal density of the target decreases, eventually making it transparent for radiation and effectively terminating the RPA. Using a circularly polarized laser [39] and plasma mirrors for reduced absorption and better laser contrast can relax some of these issues and reduce the intensity threshold to trigger RPA. Then, when the tightly-focused main pulse ( $> 10^{20} \text{ W cm}^{-2}$ ) interacts with the ultra-thin foil, finite size spot effects and transverse expansion of the plasma can also cause the maximum electron density to rapidly decrease [28, 40]. Moreover, because of the increased electron inertia due to relativistic effect, the plasma frequency decreases below the laser frequency, allowing light to propagate further inside the target and causing the occurrence of RIT [34]. The onset for this transparency regime [41, 42] is limiting the foil boost for the RPA mechanism, but can however lead to efficient ion acceleration via volumetric heating of the electrons as the target becomes transparent, therefore efficiently accelerating ions from the bulk material volume. Acceleration of ions after transparency onset played an important role in explaining observed high energy aluminum ions at the same laser facility as this work [35]. Here the transparency onset also leads to the development of self-organizing field structures at the target rear-side when the laser breaks through the target, that we further identify in our simulations to play a major role in accelerating the heavier titanium ions with low divergence and narrow spectral peaks.

Here we report on the acceleration of nearly collimated and quasi-monoenergetic titanium ions in two populations: (i) along target normal at  $\approx 0^\circ \pm 1^\circ$  and (ii) off-axis at  $\approx 11^\circ \pm 1^\circ$ , yielding respectively  $\text{Ti}^{20+}$  ions peaking at  $\sim 145 \text{ MeV}$  and multiple lower ionization states (mostly  $\text{Ti}^{15+}$  and  $\text{Ti}^{18+}$ ) peaking at a slightly higher energy of  $\sim 180 \text{ MeV}$ . The underlying ionization and acceleration mechanisms forming the on- and off-axis peaks are investigated using 2D particle-in-cell (PIC) simulations with particle tracking methods. We obtained similar energy and directionality as in the experiment with a similar optimum for the 100 nm thickness. The simulation results reported here show that the ionization and acceleration processes are divided into two stages. Before the laser breaks through the target, the fields at the target rear-side are those of TNSA. After the laser breaks through, ions can be rapidly ionized to higher charge states ( $20+$ ) by the laser field and be progressively accelerated by self-generated persisting fields for a longer time ( $\sim 2 \text{ ps}$  after the TNSA stage), yielding also an energy and an angular squeezing of ions. This mechanism, which results in formation of quasi-monoenergetic ions, relies on the long acceleration time of relatively heavy titanium ions and has not been reported in the literature for lighter ions [32, 35, 36].

## 2. Methods and results

### 2.1. Laser system and ion diagnostics

The experiment was performed using the Nd:glass Trident laser delivering 75 J during 650 fs at 1.054  $\mu\text{m}$  wavelength. The laser pedestal drops below the detection threshold  $< 10^{-9}$  nearly 50 ps before the main pulse and is  $10^{-8}$  nearly 10 ps before the main pulse [35, 43]. The laser contrast is undoubtedly crucial for efficient heavy-ion acceleration from ultra-thin targets [44]. In [35], the authors show that the Trident laser contrast was good enough to preserve the integrity of a 250 nm carbon foil (same linear density as a 60 nm titanium foil) and carbon spectral peaks were generated via a similar RIT-enhanced mechanism. The expansion of a low-density plasma in front of the target may move the critical density ahead by a few microns and expedite the transparency of the target by a few tens of fs, albeit probably without modifying drastically the characteristics of the acceleration and spectral peak formation discussed here for a 100 nm titanium foil. The laser is focused by an  $f/3$  off-axis parabola to a 4.5  $\mu\text{m}$  focal spot (FWHM) at normal incidence onto a ultra-thin foil of titanium of different thicknesses (60, 80, 100 and 140 nm). The ions created by the interaction of this laser with the target were collected by iWASP [45] and Thomson Parabolas spectrometers [46, 47] (figure 1(a)). The iWASP is composed of a slit coupled with a magnetic field parallel to it, allowing the magnetic deflection depending on the  $q/A$  and energy of the ions at different angles. It was placed 1 cm away from the rear side of the target and provide angular information concerning the ions accelerated by the laser-target interaction between  $-22.5^\circ$  and  $+22.5^\circ$ . Two Thomson Parabolas (TP) were placed at  $0^\circ$  and  $11^\circ$  attached to the chamber wall collecting ions within a solid angle of  $3.4 \times 10^{-8}$  steradians (sr). The alignment angle error can be estimated as  $\pm 1^\circ$ . The TP comprises

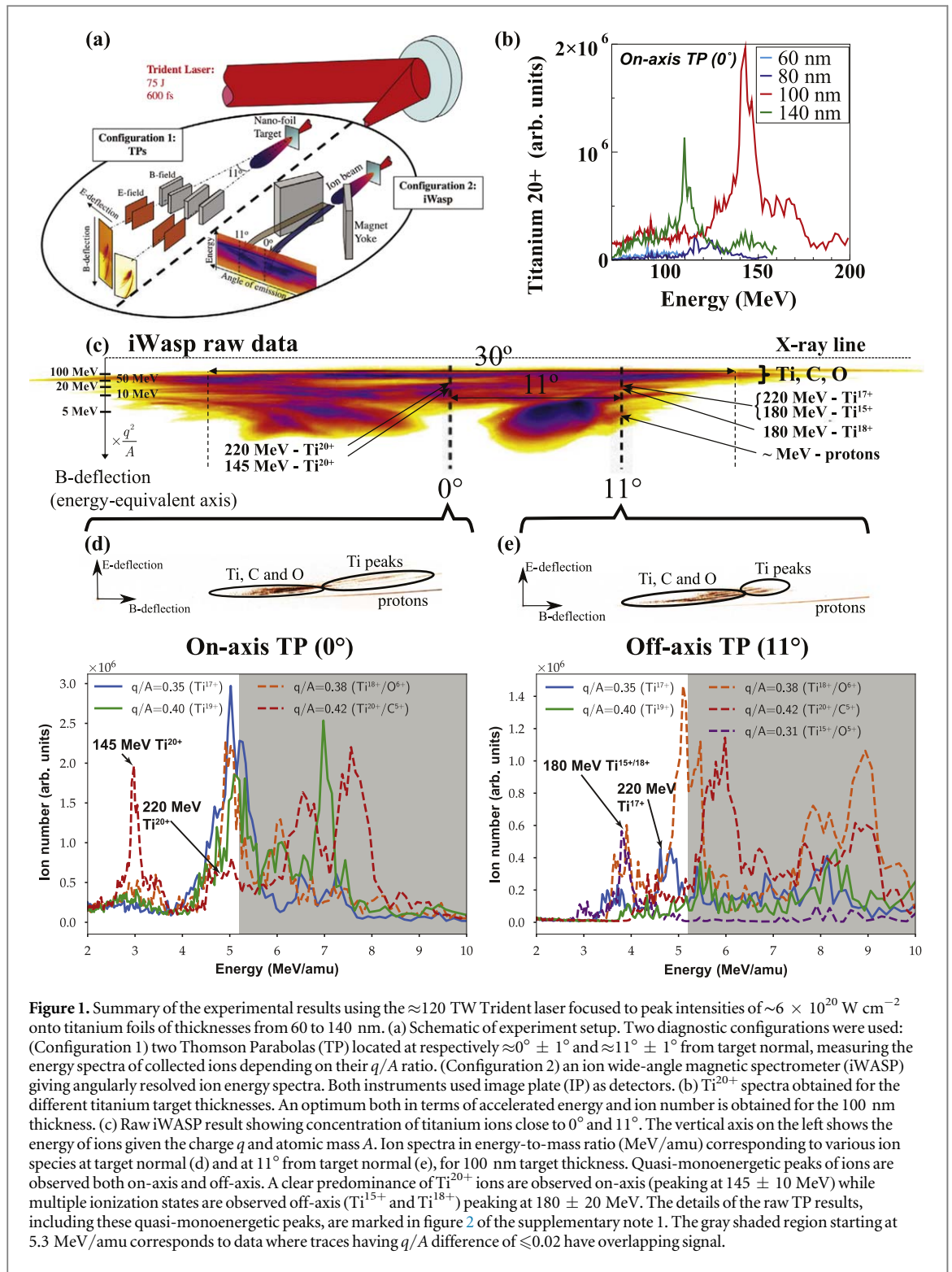


**Figure 1.** Summary of the experimental results using the  $\approx 120$  TW Trident laser focused to peak intensities of  $\sim 6 \times 10^{20} \text{ W cm}^{-2}$  onto titanium foils of thicknesses from 60 to 140 nm. (a) Schematic of experiment setup. Two diagnostic configurations were used: (Configuration 1) two Thomson Parabolas (TP) located at respectively  $\approx 0^\circ \pm 1^\circ$  and  $\approx 11^\circ \pm 1^\circ$  from target normal, measuring the energy spectra of collected ions depending on their  $q/A$  ratio. (Configuration 2) an ion wide-angle magnetic spectrometer (iWASP) giving angularly resolved ion energy spectra. Both instruments used image plate (IP) as detectors. (b)  $Ti^{20+}$  spectra obtained for the different titanium target thicknesses. An optimum both in terms of accelerated energy and ion number is obtained for the 100 nm thickness. (c) Raw iWASP result showing concentration of titanium ions close to  $0^\circ$  and  $11^\circ$ . The vertical axis on the left shows the energy of ions given the charge  $q$  and atomic mass  $A$ . Ion spectra in energy-to-mass ratio (MeV/amu) corresponding to various ion species at target normal (d) and at  $11^\circ$  from target normal (e), for 100 nm target thickness. Quasi-monoenergetic peaks of ions are observed both on-axis and off-axis. A clear predominance of  $Ti^{20+}$  ions are observed on-axis (peaking at  $145 \pm 10$  MeV) while multiple ionization states are observed off-axis ( $Ti^{15+}$  and  $Ti^{18+}$ ) peaking at  $180 \pm 20$  MeV. The details of the raw TP results, including these quasi-monoenergetic peaks, are marked in figure 2 of the supplementary note 1. The gray shaded region starting at 5.3 MeV/amu corresponds to data where traces having  $q/A$  difference of  $\leq 0.02$  have overlapping signal.

an electric field coupled with a magnetic field allowing the deflection of ions depending of their energy and charge over mass ratio  $q/A$ . This yields a parabolic deflection of the particles depending of their energy, that is between 10 and 700 MeV for mid-Z ions. The resolution of the TP depend of the energy  $dE \approx E^{3/2}$  of the detected particles [48], which can be approximate as  $\Delta E/E \approx 10^{-4}$  for a particle of 100 MeV energy. Ions parabolic traces are collected by an Image Plate (IP) giving a signal output in photostimulated light (PSL) which is calibrated for protons and light ions such as carbon or helium but not for heavier ions such as titanium. Details on the diagnostics and data analysis are given in the supplementary note 1, available online at [stacks.iop.org/NJP/21/103005/mmedia](http://stacks.iop.org/NJP/21/103005/mmedia).

## 2.2. Two populations of quasi-monoenergetic and near-collimated titanium ions

In figures 1(c)–(e), we show the iWASP result obtained for 100 nm thickness and the resulting spectra on TP at  $0^\circ$  and  $11^\circ$  from target normal. The iWASP signal clearly shows the emission of ions both on- and off- target axis. The off-axis population shows a peak around  $11^\circ$ , where we accordingly positioned our second TP. It is worth noting that the dark lobes in figure 1(c) at  $\sim \pm 7^\circ$  do not correspond to the off-axis titanium ions in figure 1(e). They are more likely low-energy impurities since they change significantly with target thickness, as shown in figure 1 of supplementary note 1. In figures 1(d), (e), we present the ions energy spectra in energy per nucleon (MeV/amu) for TP traces corresponding to different ratios of ion charge  $q$  to ion atomic mass  $A$ , as shown in the raw TP data on top of each figure for on-axis and off-axis respectively, with a focus on high-yield titanium ions accelerated from the target bulk. The acceleration of protons and other contaminants (C,O) are not discussed in this paper, as it results from already well-studied mechanisms in literature both for TNSA and RIT/BOA mechanisms [32–34]. However, the part of the ion spectra with an energy per nucleon greater than 5.3 has to be regarded with caution since nearby traces separated by a difference in  $q/A$  of 0.02 start to overlap. Therefore, nearby contaminant traces can contribute to the extracted signal, and as a result it is difficult to distinguish both populations on the image plate (IP) detector. The transition to the area of the spectrum where impurity traces are overlapping, at  $\approx 5.3$  MeV/amu, is highlighted in gray on the figures. In this article, we will discuss the peaks pointed by the arrows in figures 1(d) (e). Indeed, they correspond to peaks which have been identified further in simulations and belongs to a part of the spectrum where the nearby traces are distinguishable with no overlapping issue. In addition, the presence of  $\text{Ti}^{17+}$  and  $\text{Ti}^{19+}$  traces near the peaks, which cannot correspond to any contaminant, confirms the presence of titanium ions in this part of the spectrum. The part at energies  $> 5.3$  MeV/amu may also contain some pronounced peaks of titanium ions. However, they do not appear in simulations and the species are not conclusively identified from the experimental data due to overlapping of the traces. More information about species discrimination is given in the supplementary note 1.

The unfolded on-axis spectra (figure 1(d)) reveals quasi-monoenergetic titanium ions with a clear predominance of  $\text{Ti}^{20+}$  ions, peaking strongly at  $145 \pm 10$  MeV with a less pronounced peak at  $220 \pm 20$  MeV. Other ionization states identified from the other traces barely emerge from the noise. The off-axis lines (figure 1(e)) correspond to multiple titanium ionization states (from  $15+$  to  $20+$ ) with a peak at a slightly higher energy of  $180 \pm 20$  MeV for  $\text{Ti}^{15+}$  and  $\text{Ti}^{18+}$  and at  $220 \pm 20$  MeV for  $\text{Ti}^{17+}$ . The energies of these peaks approximately agree with the iWASP results in figure 1(c).

The different behaviors observed between the ionization states and energy of on-axis and off-axis ions are remarkable and indicate that the electromagnetic fields experienced by the two ion populations are effectively different. In particular, the unique monoenergetic spike of  $\text{Ti}^{20+}$  observed on-axis suggests that all the ions are strongly ionized by the optical field of the laser to  $\text{Ti}^{20+}$ . Surprisingly, for off-axis ions, despite having a slightly higher energy, the ionization levels and yields are lower. To the extent that the ionizing and accelerating fields are the same, this seems at first glance contradictory. We will show later based on numerical simulations that both on- and off-axis ions experience similar fields, but the off-axis ions are effectively accelerated for longer time and therefore achieve higher kinetic energies.

In figure 1(b), we present on-axis acceleration of  $\text{Ti}^{20+}$  ions for different target thicknesses used in the experiment (60, 80, 100 and 140 nm). It appears that the energy and number of the accelerated  $\text{Ti}^{20+}$  ions are significantly higher for the 100 nm thickness with respect to other thicknesses. Indeed, we observed very poor acceleration of titanium ions in our experimental detection range (100–200 MeV) for both 60 and 80 nm thicknesses, although a clear quasi-monoenergetic peak similar to that of 100 nm is still observed at 140 nm at  $\sim 110$  MeV, with about half number of ions. Further, we will focus on the optimum 100 nm thick target for the analysis of the acceleration processes. We discuss other thicknesses and discrepancies found between simulations and experiment in supplementary note 3.

## 2.3. Numerical modeling

### 2.3.1. Particle-in-cell simulations

The 2-dimension particle-in-cell (PIC) simulations were performed with EPOCH code [49]. The simulation domain is a rectangle with the size of  $120 \mu\text{m}$  (longitudinal) by  $40 \mu\text{m}$  (transverse), as shown in figure 2(a). The titanium foil with thicknesses of 60, 100 or 140 nm is initially located  $30 \mu\text{m}$  away from the left boundary. The initial number density of titanium atoms is  $5.64 \times 10^{28} \text{ m}^{-3}$  (the density of solid titanium). The contaminant layers with carbon, hydrogen and oxygen were put on both sides of the target with thickness of 10 nm and number density of  $4.6 \times 10^{28} \text{ m}^{-3}$ , corresponding to the CH material with density  $1 \text{ g cm}^{-3}$ . The laser pulse with wavelength of  $1 \mu\text{m}$  is launched at the left boundary at time  $t = -750$  fs and propagates along the longitudinal direction (from left to right) focused at the surface of the target foil located at  $x = 0 \mu\text{m}$ . The spatial and temporal profiles of the laser pulse are both Gaussian with the full width at half maximum (FWHM) of  $4.5 \mu\text{m}$  and 650 fs. The peak laser intensity is  $6 \times 10^{20} \text{ W cm}^{-2}$  on the focal plane at  $y = 0$  when the target is



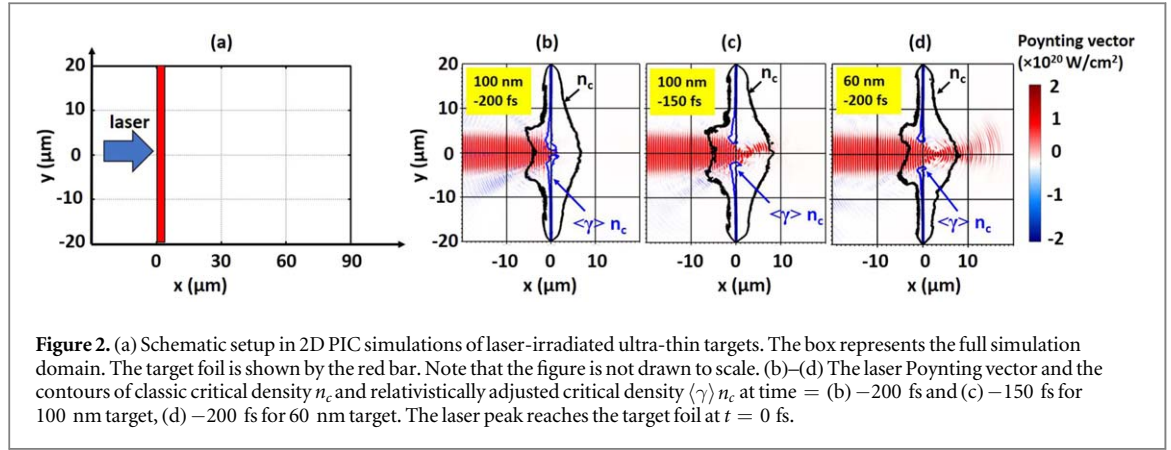


**Figure 2.** (a) Schematic setup in 2D PIC simulations of laser-irradiated ultra-thin targets. The box represents the full simulation domain. The target foil is shown by the red bar. Note that the figure is not drawn to scale. (b)–(d) The laser Poynting vector and the contours of classic critical density  $n_c$  and relativistically adjusted critical density  $\langle\gamma\rangle n_c$  at time = (b) –200 fs and (c) –150 fs for 100 nm target, (d) –200 fs for 60 nm target. The laser peak reaches the target foil at  $t = 0$  fs.

absent, and the peak reaches the target front surface at  $t = 0$  fs. We use 200 cells per wavelength along both longitudinal and transverse directions with 100 neutral particles in each cell with non-zero density at the beginning of the simulation. The boundary conditions of the simulation domain are open for both fields and particles. The field ionization packages, including barrier suppression (BSI), ADK tunneling and multiphoton ionization, are turned on in the simulations to model the ionization process of the laser-solid interaction. It is worth noting that the ADK tunneling model is based on earlier work by Perelomov, Popov and Terent'ev [50–52].

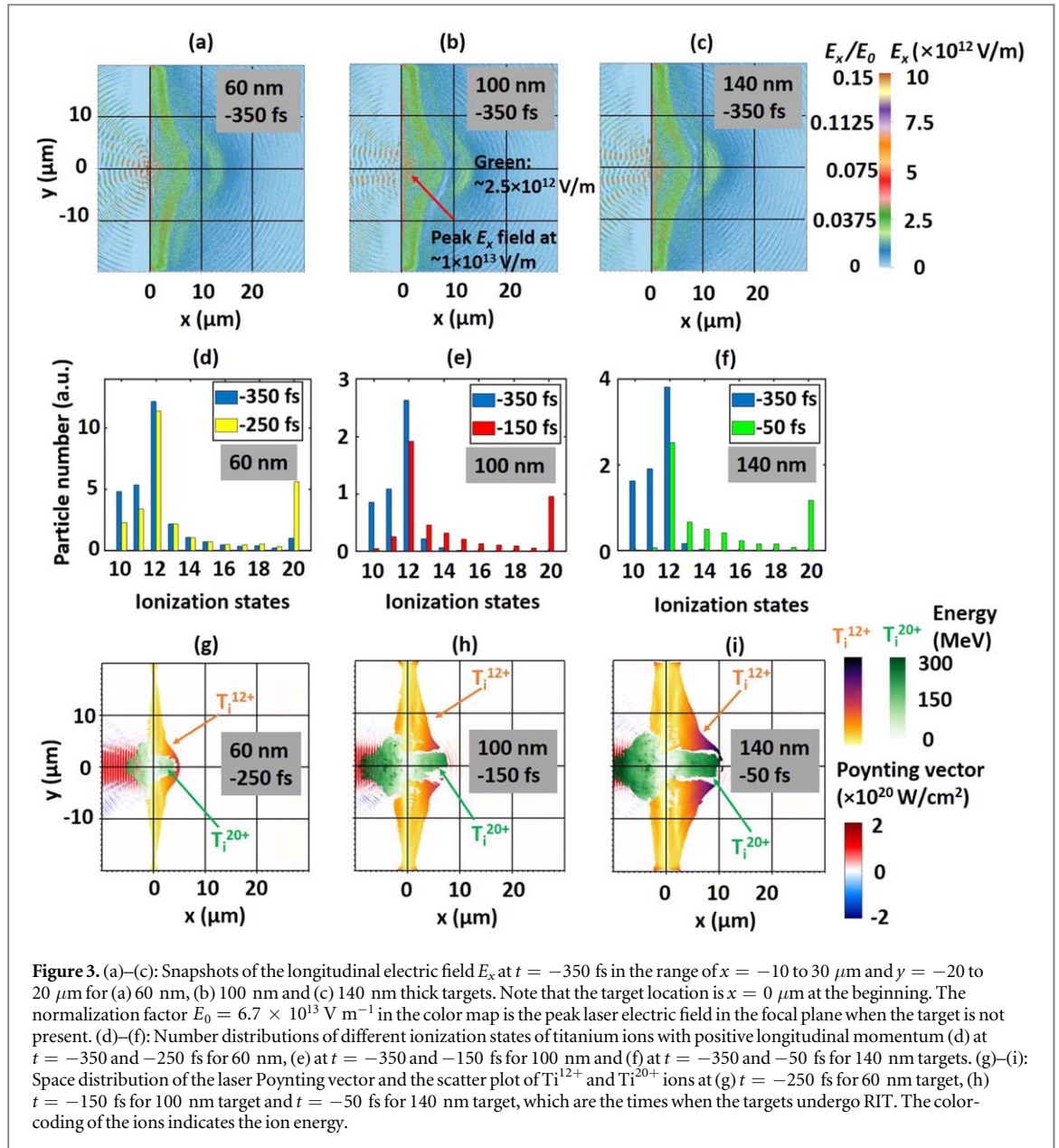
### 2.3.2. The onset of RIT

In the interaction of laser pulses with ultra-thin foils, the target transparency condition [53] can be given by  $a_0 = \pi n_e l / (n_c \lambda)$ , where  $a_0 = 0.85 \sqrt{I \lambda^2 / (10^{18} \mu\text{m}^2 \text{ W cm}^{-2})}$  is the dimensionless amplitude of the laser with intensity  $I$  and wavelength  $\lambda$ ,  $n_e$  is the electron density,  $l$  is the target thickness, and  $n_c = \epsilon_0 m_e \omega_0 / e^2$  is the critical density of the incident laser. Here  $\epsilon_0$ ,  $m_e$ ,  $e$ ,  $\omega_0$  respectively stand for the vacuum permittivity, the mass and charge of an electron, and the frequency of the incident laser. For our physical conditions,  $n_e \approx 1.1 \times 10^{30} \text{ m}^{-3}$  is calculated from solid titanium ion density and ionization state of 20+,  $n_c = 1 \times 10^{27} \text{ m}^{-3}$  for the incident laser with  $\lambda = 1 \mu\text{m}$ ,  $a_0 = 21$  for the peak laser intensity  $I = 6 \times 10^{20} \text{ W cm}^{-2}$ . With these parameters we obtain  $l = 6 \text{ nm}$  using the transparency condition formula [53], suggesting our targets with thicknesses from 60 to 140 nm should be opaque in the beginning of the interaction with high plasma density  $n_e$ . However, they can become transparent due to the rapid drop of  $n_e$  caused by target expansion during the pulse duration of hundreds of femtoseconds. Figures 2(b), (c) show the longitudinal component of the laser Poynting vector near the target locations for the 100 nm target when it becomes transparent to the laser. The contour of  $\langle\gamma\rangle n_c$  describes the effective critical density for the laser due to relativistic effects, where  $\langle\gamma\rangle$  is the average Lorentz factor of local plasma electrons. Beyond the  $\langle\gamma\rangle n_c$  boundary, the laser field evanescently decays. At  $t = -200$  fs, the laser field can penetrate through a plasma with density  $n_e$ , but drastically drops beyond  $\langle\gamma\rangle n_c$  (figure 2(b)). By  $t = -150$  fs, the laser has propagate further, as the plasma density drops below  $\langle\gamma\rangle n_c$ . By this time the plasma density has decreased by  $\sim 100$  times compared to the initial density, making it possible for the laser to propagate through a much thicker target than the 6 nm mentioned above. The onset time of RIT varies for different target thicknesses (figures 2(b)(d)). For 60 and 140 nm targets, RIT occurs at  $t = -250$  fs and  $-50$  fs respectively.

### 2.3.3. The ionization processes

The EPOCH field ionization package calculates the probabilities of field ionization for each ion based on the the electric field strength at the ion position [54]. The ionization process additionally depends on the exposure time of each ion to the electric fields. In the characteristic time scale of a few hundreds of femtoseconds in our simulations, the relation of the ionization states of titanium ions and the externally applied electric fields is studied and discussed in supplementary note 2.

Prior to RIT, titanium atoms on the rear side are ionized and accelerated via TNSA. The electric field structures for the three targets are shown in figures 3(a)–(c). They have broad similarities in terms of amplitude and spatial characteristics, with the field strength in this stage of typically  $\sim 2.5 \times 10^{12} \text{ V m}^{-1}$ , with some local strong peaks at  $\sim 1 \times 10^{13} \text{ V m}^{-1}$ . According to our discussion in supplementary note 2, an electric field of  $\sim 2.5 \times 10^{12} \text{ V m}^{-1}$  corresponds to a stable ionization state of  $\text{Ti}^{12+}$  in the time scale of hundreds of femtoseconds, while  $\sim 1 \times 10^{13} \text{ V m}^{-1}$  results in multiple ionization states above  $\text{Ti}^{13+}$ . Consequently, the titanium ions on the target rear side should be dominated by  $\text{Ti}^{12+}$  ions with some higher ionization states, but in much smaller numbers. This is illustrated in the ionization state distributions presented in figures 3(d)–(f).

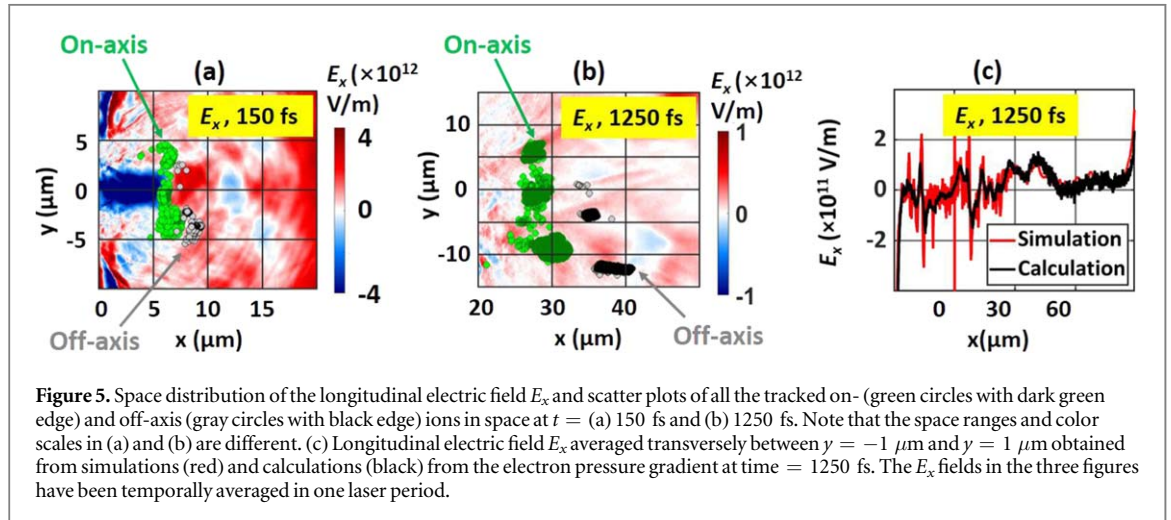
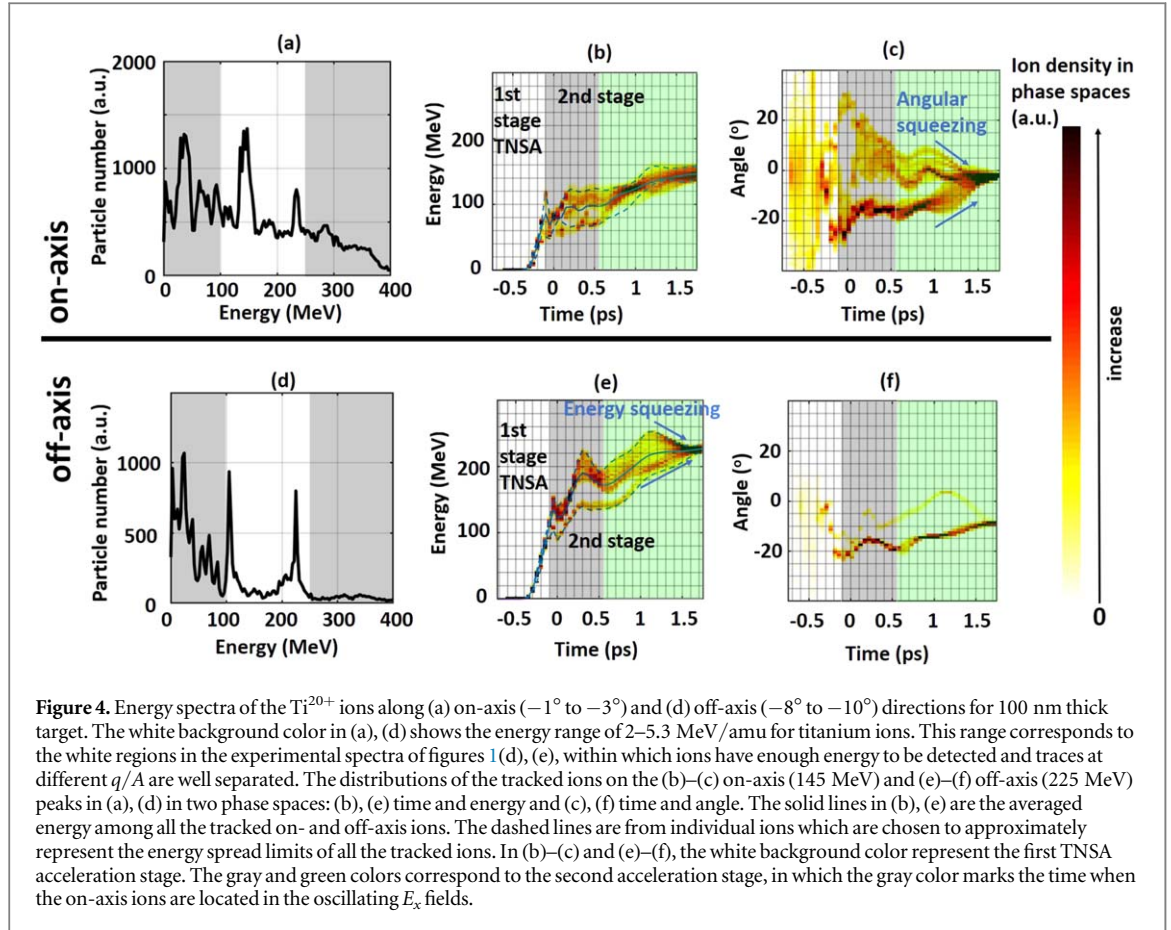


After the targets become transparent, the titanium ions located at the target center on the rear side are exposed directly to the laser electric field. The peak electric field of the laser pulse when the target is not present is  $6.7 \times 10^{13} \text{ V m}^{-1}$ . With this electric field, the ionization state should saturate at  $\text{Ti}^{20+}$  [supplementary note 2], as shown in figures 3(g)–(i). The transition from  $\text{Ti}^{12+}$  ions to  $\text{Ti}^{20+}$  after the laser breaks through the targets is also demonstrated in figures 3(d)–(f). This qualitatively explains the energy spectra of titanium ions in figures 1(d), (e) where on-axis titanium ions are dominated by  $\text{Ti}^{20+}$ , while the off-axis ions exhibit lower ionization states such as  $\text{Ti}^{15+}$  and  $\text{Ti}^{18+}$ .

#### 2.3.4. The acceleration processes

We study the acceleration of the ions in quasi-monoenergetic peaks for the 100 nm thick target, as measured in the experiment and shown in figures 1(d)–(e). The PIC simulation with 100 nm target at the end of the simulation ( $t = 1750$  fs) shows quasi-monoenergetic  $\text{Ti}^{20+}$  ions at 145 MeV and a smaller peak at 230 MeV, near target normal direction (on-axis,  $-1^\circ > \theta > -3^\circ$ ) in figure 4(a). It also shows a peak at 225 MeV along the off-axis direction ( $-8^\circ > \theta > -10^\circ$ ) in figure 4(d). Both fairly agrees with the experimental results for the ions accelerated in the on- and off-axis directions. Here the angle  $\theta$  is defined as  $\theta = \arctan(p_y/p_x)$ , where  $p_y$  and  $p_x$  are the transverse and longitudinal momenta of the accelerated ions. Particle tracking analysis was performed to follow *how* and *when* these ions are accelerated. Specifically, we tracked the  $\text{Ti}^{20+}$  ions within narrow energy ranges (132 to 159 MeV for on-axis, and 216 to 231 MeV for off-axis) and angle ranges ( $-1^\circ > \theta > -3^\circ$  for on-axis and  $-8^\circ > \theta > -10^\circ$  for off-axis) at the end of the simulation. In total there are 9430 and 1850 ions in the





chosen energy and angle ranges for on- and off-axis peaks at  $t = 1750$  fs respectively, and all of these ions are tracked through the entire simulation. The tracked information is mapped in the phase spaces of time, energy and angle in figure 4. Their locations in the simulation domain at different times will be presented in figure 5.

The energy histories of the tracked on- and off-axis ions in figures 4(b), (e) clearly illustrate two acceleration stages with a transition from  $t = -100$  to  $-50$  fs, which is about 50–100 fs after the occurrence of RIT. In the first acceleration stage, all the tracked ions are located close to the target rear side and accelerated by the strong TNSA sheath field, resulting in the first steep slopes of the first stage and yielding significant energy gains of 85–140 MeV on average, as shown by the solid curves in white background regions of figures 4(b), (e).

Immediately after the onset of RIT, the laser drills a ‘channel’ in the plasma and an energetic electron beam is formed along the channel propagating to the target rear side [35]. Oscillating longitudinal electric fields [55, 56]  $E_x$  are generated in the channel, as shown in figure 5(a). The tracked on-axis ions are located in and are affected by these fields between  $t = -150$  and 550 fs. The amplitude of these fields ( $\sim 10^{12} \text{ V m}^{-1}$ ) are comparable to the

TNSA sheath field in the first stage, but they contribute to only a small amount ( $\sim 10$  MeV = 7%) of the total energy gain of 145 MeV of the on-axis ions, as shown by the solid curve in the gray background region of figure 4(b). The reason is that these  $E_x$  fields oscillate over a much shorter period (100–200 fs) than the entire duration of 700 fs (from  $t = -150$  to 550 fs).

The off-axis ions are not affected by the oscillating  $E_x$  fields since they leave the fields region between  $y = -3$  and  $3 \mu\text{m}$  after  $t = 50$ – $150$  fs, as shown in figure 5(a). Consequently, they are still accelerated by the  $E_x$  fields in the expanding plasma and gain energy more efficiently than the on-axis ions. During this period from  $t = -150$  to 550 fs, the off-axis ions gain  $\sim 37$  MeV = 17% of the off-axis final energy 225 MeV (the gray region in figure 4(e)). In contrast to the on-axis ions, the off-axis ions are more effectively accelerated during this period, while the acceleration of on-axis ions is inhibited. This difference suggests longer effective acceleration time for off-axis ions than on-axis ions, which can cause higher energy of the off-axis ions, as observed in the experiments. One may notice that a deceleration phase can be observed right after  $t = 250$  fs. It results from the negative longitudinal electric field caused by the local electron pressure gradient in the expanding plasma. This mechanism of generating electric field is also responsible for the ion acceleration in the late stage, as we discuss in the following paragraphs.

From  $t = 550$  fs to the end of the simulation at  $t = 1750$  fs [the light green background regions of figure 4(b)(e)], both the on- and off-axis ions gain  $\sim 50$  MeV from the self-generated electric field, which is referred to as ‘remaining field’, as shown in figure 5(b). The generation of the remaining electric field can be roughly explained by the local electron pressure gradient with the assumption of thermal equilibrium. At  $t = 550$  fs, the laser intensity has decreased to  $\sim 10\%$  of the peak value. This value drops to  $\sim 1\%$  later at  $t = 1000$  fs. Without the strong laser pump, the physics in the expanding plasma can be described by a plasma free expansion model, in which the electric field on the electrons are mainly generated by the electron pressure gradient  $E_x = -\frac{\nabla P_e}{|e|n_e} \approx -\frac{\nabla(n_e T_e)}{|e|n_e}$ , where  $T_e$  and  $P_e$  are respectively the electron temperature and pressure in space. We calculated the  $E_x$  field along  $x$  axis averaged transversely between  $y = -1 \mu\text{m}$  and  $1 \mu\text{m}$  at  $t = 1250$  fs, and the results agree well with the electric field obtained directly from the simulation (figure 5(c)), especially in the region of  $x < 40 \mu\text{m}$  where the tracked particles are located.

The remaining electric field is about 10 times weaker than the TNSA field in the first stage. However, we observed in figures 4(b), (e) comparable energy gains for both stages. Estimates can be made as follows. We assume  $E_x$  is  $2 \times 10^{11}$  V m $^{-1}$ , one order of magnitude smaller than the TNSA sheath field in the first stage, and a  $\text{Ti}^{20+}$  ion moving along the field direction is injected in the field with initial energy of 100 MeV, or velocity of  $2 \times 10^7$  m s $^{-1}$ . After 1 ps, the energy gain of the  $\text{Ti}^{20+}$  ion is 95 MeV, the same order as the energy gain in the simulations. The somewhat lower energy gain obtained in simulation is certainly caused by the temporal decay of  $E_x$ , which is not taken into account in our simple estimate. Yet, we showed that although the remaining electric field is weak, it can significantly contribute to the ion energy gain.

### 2.3.5. The formation of the quasi-monoenergetic peaks

The quasi-monoenergetic peaks for the 100 nm thick target are formed in the late stage of the simulation after  $t = 1000$  fs. The formation mechanisms can be inferred from the time evolution of angular and energy distributions of the tracked titanium ions. The energy spread of the tracked on-axis ions does not change much after  $t = 1000$  fs (figure 4(b)), but their angular spread decreases significantly from  $30^\circ$  at  $t = 1000$  fs to  $2^\circ$  at the end of the simulation (figure 4(c)). This angular accumulation results from the squeezed  $p_y$  of these ions caused by the transverse electric fields  $E_y$ , as demonstrated in figure 6(a). Besides the filaments structure of  $E_y$  near  $y < 5 \mu\text{m}$  caused by the beams of ions and electrons (figure 6(b)), in the region with  $|y| > 5 \mu\text{m}$ , the tracked on-axis ions with negative  $p_y$  (blue circles) are mainly located in positive  $E_y$  (red background), and vice versa. This results in a significant transverse focusing effect on the titanium ions. The time evolution of the  $E_y$  fields is plotted in figure 6 of the supplementary note 4, which shows that the global collimating fields at  $|y| > 5 \mu\text{m}$  are temporally stable. The  $E_y$  fields can be caused by the transverse electron pressure gradient. As discussed in the last section, the electric fields in the late stage are remaining electric fields that can be explained by the pressure gradient of the electrons. Figure 6(b) shows the density distribution of electrons at  $t = 1250$  fs. In the region with  $x \sim 30 \mu\text{m}$  and  $|y| > 5 \mu\text{m}$ , the plasma density is higher on the sides but lower for smaller  $y$ . This transverse density gradient contributes to transverse electron pressure gradient and the collimating  $E_y$  fields.

The angular and energy spreads of the tracked off-axis ions show the opposite features to the on-axis ions. In the angular space (figure 4(f)), the off-axis ions have small angular spread ( $\sim 5^\circ$ ) very early after the TNSA stage, and the  $E_y$  fields on the off-axis ions mainly have positive components (gray circles with black edge in figure 6(a)), which cannot collimate ions. In the energy space, their energy spread decreases significantly from 60 MeV to 16 MeV (figure 4(e)) after  $t = 1000$  fs, suggesting an energy squeezing effect. This effect is illustrated in figure 5(b) that the  $E_x$  fields on the off-axis ions include both positive and negative components ( $\sim 10^{11}$  V m $^{-1}$

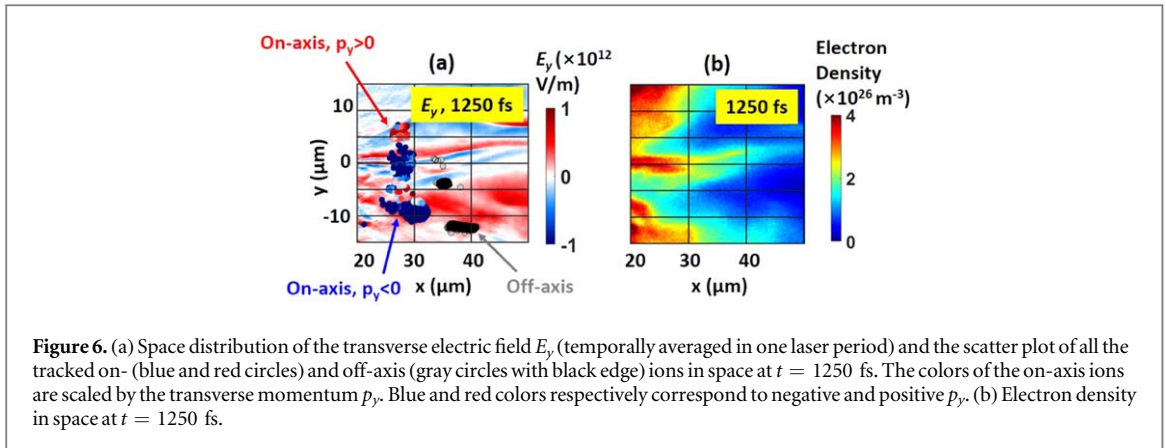


**Figure 6.** (a) Space distribution of the transverse electric field  $E_y$  (temporally averaged in one laser period) and the scatter plot of all the tracked on- (blue and red circles) and off-axis (gray circles with black edge) ions in space at  $t = 1250$  fs. The colors of the on-axis ions are scaled by the transverse momentum  $p_y$ . Blue and red colors respectively correspond to negative and positive  $p_y$ . (b) Electron density in space at  $t = 1250$  fs.

near  $x \sim 40 \mu\text{m}$  and  $y \sim -10 \mu\text{m}$ ), and the negative  $E_x$  fields can slow down the faster Ti ions and squeeze the ions in energy. Within the peak formation time scale of 500 fs, the negative field  $E_x = -1 \times 10^{11} \text{ V m}^{-1}$  can reduce the energy of 250 MeV  $\text{Ti}^{20+}$  ions by  $\sim 30$  MeV, which is approximately half the energy spread change for the off-axis ions after  $t = 1000$  fs. The negative  $E_x$  fields are generated in the region  $x > 40 \mu\text{m}$  and  $y < -5 \mu\text{m}$  by the negative electron density gradient in the same region (figure 6(b)). Due to the squeezing effect, these ions accumulate in the energy space after  $t = 1000$  fs and form the off-axis quasi-monoenergetic peak.

### 3. Discussion and conclusion

The two mechanisms discussed above rely on the long acceleration time ( $\sim 2$  ps) of titanium ions in the remaining field of the second stage, which is the most significant difference between the acceleration of titanium ions and lighter ions including carbon, hydrogen and aluminum [32, 35, 36] in previous research. The lighter ions leave the target too early to benefit from a second stage because they are rapidly ionized to high charge states; ions from surface impurities are further disadvantaged by their location. Thus, they are not so strongly affected by the remaining field compared to heavier ions such as titanium. In particular, previous experiments with similar laser parameters have shown that the target aluminum atoms are ionized to high charge states early so that they can be initialized as  $\text{Al}^{11+}$  (close to fully-ionized) in the PIC simulations [35] without losing essential physics. By contrast, the titanium ions are only about half-ionized ( $\text{Ti}^{12+}$ ) before the onset of RIT in our study. This difference limits the speed of the titanium ions and prolongs their acceleration duration, which enables the peak formation mechanisms in the late stage.

In this article, we demonstrate the generation of high-quality, high charge state titanium ion beams, which are important markers for the advancement of the field of laser-accelerated ions. PIC simulations indicate a two-stage acceleration of the ions before and after the onset of RIT. These ions are first accelerated through the TNSA mechanism and are further boosted by the self-generated persisting electric field in the expanding plasma for a longer time beyond the laser pulse duration ( $\sim 2$  ps after the TNSA stage), causing the formation of the quasi-monoenergetic peaks observed in the simulation and measured experimentally. The results show the important role of the self-generated fields in the ion beam generation. First, even after the laser-target interaction, ions can still be accelerated efficiently by the self-generated fields and gain comparable energy to that achieved during the interaction. Second, these fields can squeeze the ion beams in both energy and angle to significantly improve the ion beam quality. These findings could be applied in future ion acceleration experiments on the numerous high-power laser facilities being constructed presently. As a matter of fact, considering lasers with intermediate pulse duration from 500–1000 fs and multi-petawatt power, we expect enhanced acceleration in both stages, i.e. higher sheath field for the first TNSA stage and higher electron pressure gradient for the second stage. Moreover, higher power lasers allow for thicker targets to trigger the RIT onset near the laser pulse peak, thereby relieving from the demanding high contrasts needed to preserve the target integrity. It is noteworthy that for RPA mechanisms at higher power, more stringent contrast ratios would conversely be needed.

### Acknowledgments

We acknowledge useful discussions with Dr A Higginson. This work is supported by the Air Force Office of Scientific Research under award number FA9550-14-1-0282 and the University of California Office of the President Lab Fee under grant number LFR-17-449059. The work of SSB was supported by U.S. DOE under Contract No. DE-AC02-05CH11231. The work of AVA was supported by the US Department of Energy under

contract No. DE-SC0018312. This work was performed using HPC resources provided by the Texas Advanced Computing Center at the University of Texas and the San Diego Supercomputer Center at the University of California, San Diego. This work used the Extreme Science and Engineering Discovery Environment (XSEDE) [57], which is supported by National Science Foundation grant number ACI-1548562. We appreciate the hard work of the Trident laser operators T Shimada and R Gonzales.

## ORCID iDs

J Li  <https://orcid.org/0000-0001-9247-0760>

M Bailly-Grandvaux  <https://orcid.org/0000-0001-7529-4013>

A V Arefiev  <https://orcid.org/0000-0002-0597-0976>

A E Hussein  <https://orcid.org/0000-0001-9676-4862>

F N Beg  <https://orcid.org/0000-0003-0391-8944>

## References

- [1] Mourou G A, Tajima T and Bulanov S V 2006 *Rev. Mod. Phys.* **78** 309–71
- [2] Daido H, Nishiuchi M and Pirozhkov A S 2012 *Rep. Prog. Phys.* **75** 056401
- [3] Macchi A, Borghesi M and Passoni M 2013 *Rev. Mod. Phys.* **85** 751–93
- [4] Patel P K, Mackinnon A J, Key M H, Cowan T E, Foord M E, Allen M, Price D F, Ruhl H, Springer P T and Stephens R 2003 *Phys. Rev. Lett.* **91** 125004
- [5] Snavely R A et al 2007 *Phys. Plasmas* **14** 092703
- [6] Dyer G M et al 2008 *Phys. Rev. Lett.* **101** 015002
- [7] Koenig M et al 2005 *Plasma Phys. Control. Fusion* **47** B441–9
- [8] Collins G W, Da Silva L B, Celliers P, Gold D M, Foord M E, Wallace R J, Ng A, Weber S V, Budil K S and Cauble R 1998 *Science* **281** 1178–81
- [9] Guillot T 1999 *Science* **286** 72–7
- [10] Remington B A, Cavallo R M, Edwards M J, Ho D D M, Lasinski B F, Lorenz K T, Lorenzana H E, Mcnaney J M, Pollaine S M and Smith R F 2005 *Astrophys. Space Sci.* **298** 235–40
- [11] Huser G, Koenig M, Benuzzi-Mounaix A, Henry E, Vinci T, Faral B, Tomasini M, Telaro B and Batani D 2005 *Phys. Plasmas* **12** 060701
- [12] Koenig M et al 2010 *High Energy Density Phys.* **6** 210–4
- [13] Roth M et al 2001 *Phys. Rev. Lett.* **86** 436–9
- [14] Hegelich B M et al 2011 *Nucl. Fusion* **51** 83011
- [15] Bangerter R O 2014 *Nucl. Instrum. Methods Phys. Res. A* **733** 216–9
- [16] Clark E L, Krushelnick K, Zepf M, Beg F N, Tatarakis M, Machacek A, Santala M I K, Watts I, Norreys P A and Dangor A E 2000 *Phys. Rev. Lett.* **85** 1654–7
- [17] Petrov G M, McGuffey C, Thomas A G, Krushelnick K and Beg F N 2016 *Phys. Plasmas* **23** 063108
- [18] Braenzel J, Andreev A A, Platonov K, Klingsporn M, Ehrentraut L, Sandner W and Schnürer M 2015 *Phys. Rev. Lett.* **114** 124801
- [19] Nishiuchi M et al 2015 *Phys. Plasmas* **22** 33107
- [20] Pompos A, Durante M and Choy H 2016 *JAMA Oncology* **2** 1539–40
- [21] McKenna P et al 2003 *Phys. Rev. Lett.* **91** 075006
- [22] McKenna P et al 2004 *Phys. Rev. E* **70** 036405
- [23] Habs D, Thirolf P G, Gross M, Allinger K, Bin J, Henig A, Kiefer D, Ma W and Schreiber J 2011 *Appl. Phys. B* **103** 471–84
- [24] Wilks S C, Langdon A B, Cowan T E, Roth M, Singh M, Hatchett S, Key M H, Pennington D, MacKinnon A and Snavely R A 2001 *Phys. Plasmas* **8** 542–9
- [25] Snavely R A et al 2000 *Phys. Rev. Lett.* **85** 2945–8
- [26] Hatchett S P et al 2000 *Phys. Plasmas* **7** 2076
- [27] Esirkepov T, Borghesi M, Bulanov S V, Mourou G and Tajima T 2004 *Phys. Rev. Lett.* **92** 175003
- [28] Bulanov S S, Esarey E, Schroeder C B, Bulanov S V, Esirkepov T Z, Kando M, Pegoraro F and Leemans W P 2016 *Phys. Plasmas* **23** 056703
- [29] Henig A et al 2009 *Phys. Rev. Lett.* **103** 245003
- [30] Kar S et al 2012 *Phys. Rev. Lett.* **109** 185006
- [31] Scullion C et al 2017 *Phys. Rev. Lett.* **119** 054801
- [32] Yin L, Albright B J, Hegelich B M and Fernández J C 2006 *Laser Part. Beams* **24** 291–8
- [33] Henig A et al 2009 *Phys. Rev. Lett.* **103** 045002
- [34] Palaniyappan S et al 2012 *Nat. Phys.* **8** 763–9
- [35] Palaniyappan S, Huang C, Gautier D C, Hamilton C E, Santiago M A, Kreuzer C, Sefkow A B, Shah R C and Fernández J C 2015 *Nat. Commun.* **6** 10170
- [36] Higginson A et al 2018 *Nat. Commun.* **9** 724
- [37] Gonzalez-Izquierdo B et al 2016 *Nat. Phys.* **12** 502–12
- [38] Gonzalez-Izquierdo B et al 2016 *Nat. Commun.* **7** 12891
- [39] Qiao B, Zepf M, Borghesi M and Geissler M 2009 *Phys. Rev. Lett.* **102** 145002
- [40] Dollar F et al 2012 *Phys. Rev. Lett.* **108** 175005
- [41] Sgattoni A, Londrillo P, MacChi A and Passoni M 2012 *Phys. Rev. E* **85** 36405
- [42] Bulanov S S, Schroeder C B, Esarey E and Leemans W P 2012 *Phys. Plasmas* **19** 093112
- [43] Flippo K A et al 2013 *Eur. Phys. J. Web Conf.* **59** 07003
- [44] McGuffey C et al 2016 *New J. Phys.* **18** 113032
- [45] Jung D et al 2011 *Rev. Sci. Instrum.* **82** 043301
- [46] Thomson J 1911 *Philos. Mag.* **21** 225–49

- [47] Weber R, Balmer J E and Ladrach P 1986 *Rev. Sci. Instrum.* **57** 1251–3
- [48] Schillaci F et al 2014 *J. Instrum.* **9** T10003
- [49] Arber T D et al 2015 *Plasma Phys. Control. Fusion* **57** 113001
- [50] Popov V S 2004 *Phys.—Usp.* **47** 855–85
- [51] Mulser P and Bauer D 2010 *High Power Laser-Matter Interaction* (Berlin: Springer) (<https://doi.org/10.1007/978-3-540-46065-7>)
- [52] Perelomov A, Popov V and Terent'ev M 1966 *Sov. Phys. JETP* **23** 924
- [53] Vshivkov V A, Naumova N M, Pegoraro F and Bulanov S V 1998 *Phys. Plasmas* **5** 2727–41
- [54] Li J, Arefiev A V, Bulanov S S, Kawahito D, Bailly-Grandvaux M, Petrov G M, McGuffey C and Beg F N 2019 *Sci. Rep.* **9** 666
- [55] Powell H W et al 2015 *New J. Phys.* **17** 103033
- [56] Albright B J, Yin L, Bowers K J, Hegelich B M, Flippo K A, Kwan T J and Fernandez J C 2007 *Phys. Plasmas* **14** 094502
- [57] Towns J et al 2014 *Comput. Sci. Eng.* **16** 62–74